

NUMERICAL SOLUTION OF THE THREE-DIMENSIONAL FLUID FLOW IN A ROTATING HETEROGENEOUS POROUS CHANNEL

MARK A. HAVSTAD^a AND PETER VADASZ^{b,*}

^a *Lawrence Livermore National Laboratory, L-470, Livermore, CA 94550, USA*

^b *Department of Mechanical Engineering, University of Durban-Westville, Private Bag X54001, Durban 4000, South Africa*

SUMMARY

A numerical solution to the problem of the three-dimensional fluid flow in a long rotating heterogeneous porous channel is presented. A co-ordinate transformation technique is employed to obtain accurate solutions over a wide range of porous media Ekman number values and consequent boundary layer thicknesses. Comparisons with an approximate asymptotic solution (for large values of Ekman number) and with theoretical predictions on the validity of Taylor–Proudman theorem in porous media for small values of Ekman number show good qualitative agreement. An evaluation of the boundary layer thickness is presented and a power-law correlation to Ekman number is shown to well-represent the results for small values of Ekman number. The different three-dimensional fluid flow regimes are presented graphically, demonstrating the distinct variation of the flow field over the wide range of Ekman numbers used. Copyright © 1999 John Wiley & Sons, Ltd.

KEY WORDS: rotating flow; heterogeneous porous media; Coriolis acceleration; secondary circulation

1. INTRODUCTION

The study of flow in rotating porous media is motivated by practical applications in the food process industry, chemical process industry, centrifugal filtration processes and rotating machinery. A review of the field, including a detailed discussion of engineering applications is presented by Vadasz [1].

More specifically, packed bed mechanically agitated vessels are used in the food processing and chemical engineering industries in batch processes. The packed bed consists of solid particles or fibers of material that form the solid matrix while fluid flows through the pores. As the solid matrix rotates, due to the mechanical agitation, a rotating frame of reference is a necessity when investigating these flows. The role of the flow of fluid through these beds can vary from drying processes to extraction of soluble components from the solid particles. The molasses in centrifugal crystal separation processes in the sugar milling industry and the extraction of sodium alginate from kelp are just two examples of such processes.

Another important application of rotating flows in porous media is in the design of a multi-pore distributor in a gas–solid fluidized bed. A multi-pore distributor is a device that is

* Correspondence to: Department of Mechanical Engineering, University of Durban-Westville, Private Bag X54001, Durban 4000, South Africa.

constructed from foraminous materials, wire compacts, filter cloth, compressed fibers, sintered metal, or such like (Whitehead [2]). Research results (Davidson and Harrison [3]) showed that the porous distributor allowed a more even expansion of the bed than the other distributors and its design affected the behaviour of the bed over most of its height. An even distribution of the gas is necessary to avoid instability in the fluidized bed, which can cause the breakdown of proper fluidization. A commonly used solution to avoid maldistribution of gas and bed instability is cyclic interchange fluidization (CIF) (Kvasha [4]), where the distributor is rotating at constant angular velocities that vary between 20 and 2500 rpm, depending on the size of the bed (the higher its diameter, the lower the angular velocity). Some examples of applications of the CIT are the highly exothermic synthesis of alkylchlorosilanes polymer filling of composites, treatment of finely dispersed solids, drying of paste-like polymers, permanganate of potash and iodine (Kvasha [4]). Therefore, evaluating the flow field through a porous rotating distributor becomes a design necessity.

The macro-level porous media approach is gaining an increased level of interest in solving practical fluid flow problems that are too difficult to solve by using a traditional micro-level approach. As such, direct chill (DC) casting models apply the Darcy law to predict the heat transfer, fluid flow and ultimately the thermal stresses in the solidified metal. Such a model was applied by Katgerman [5] to analyze the heat transfer phenomena during continuous casting of aluminium alloys. When centrifugal casting processes are considered, rotation effects become relevant to the problem. The porous medium approach is also used in processing of composite materials. Güçeri [6] states that 'most of the studies of resin transfer molding (RTM) processes and structural reaction injection molding (SRIM) treat the flow domain as an anisotropic porous medium and perform a Darcy flow analysis utilizing a continuum model'.

Additional applications of the porous medium approach are discussed by Nield and Bejan [7] and Bejan [8] in comprehensive reviews of the fundamentals of heat convection in porous media. Bejan [8] mentions among the applications of heat transfer in porous media the process of cooling of winding structures in high-power density electric machines. When this applies to a rotor of an electric machine, say generator (or motor), a problem of a current industrial interest, rotation effects become relevant as well. Additional recent applications of the porous media approach are the flow of liquids in biological tissues like the human brain, the cardiovascular flow of blood in the human heart or other physiological processes, pebble-bed nuclear reactors and cooling of turbine blades in the hot portion of a turbo-expander. Regarding the last application, such a cooling process enables the expander inlet gas temperature to increase beyond the allowed metal temperature, bringing a significant contribution to the cost-effectiveness of the expander. The cooling process occurs by injecting air through channels in the internal part of the blade. As long as the geometry of the channels is not too complicated, the traditional heat transfer approach can be applied to evaluate the cooling performance. However, for complicated channel geometry, the porous medium approach will prove again the most effective way of simulating the phenomenon.

With the emerging utilization of the porous medium approach in non-traditional fields, including some applications in which the solid matrix is subjected to rotation (like physiological processes in human body subject to rotating trajectories, or cooling of rotors of electric machines) a thorough understanding of the flow in a possibly anisotropic or heterogeneous rotating porous medium becomes essential. Its results can then be used in the more established industrial applications, like food processes, chemical engineering or centrifugal processes, as well as to the aforementioned non-traditional applications of the porous medium approach.

Rotation in isothermal flows in porous media has received relatively little attention, because *isothermal flow in homogeneous porous media following Darcy's law is irrotational* (Bear [9]). However, for a heterogeneous medium or for free convection in a non-isothermal homogeneous porous medium the flow is not irrotational and the effects of rotation become significant. In some applications, these effects can be small, e.g. when the porous media Ekman number is high. For high angular velocities of rotation or extremely high permeabilities (conditions pertaining to some engineering applications), the Ekman number can become of unit order of magnitude or lower and then the effect of rotation is enhanced. The effect of rotation is of particular interest for its tendency to generate secondary flows in planes perpendicular to the main flow direction (even when these secondary flows are weak, it is essential to understand their source). While each industrial application needs special attention and particular models including complicated combinations of the relevant effects need to be developed separately, it is of paramount importance to understand the underlying theory behind these effects prior to attempting to formulate and solve the complicated models.

The fundamental theoretical aspects of such flows, including the proof of the existence of Taylor–Proudman columns in porous media, and their experimental confirmation, was presented by Vadasz [1]. These results apply to small values of the porous media Ekman number. One of the conclusions from this study was that the flow at high rotation rates (small Ekman numbers) has a tendency towards two-dimensionality, leading to a flow in the plane perpendicular to the rotation axis. On the other hand, the effect of rotation on the flow through heterogeneous porous media in a rotating square channel was investigated analytically by Vadasz [10], for the case of small rotation rates (i.e. large values of the porous media Ekman number), while using an asymptotic method of solution. The major conclusion from this study was that the axial flow in a heterogeneous porous channel is deflected due to rotation and secondary circulation is produced in a plane perpendicular to the imposed axial flow. However, the limitation of the results presented by Vadasz [10] to small rotation rates ($Ek \gg 1$) and the asymptotic method used, which produces approximate results, motivates the present study where accurate results over a wide range of Ekman number values are sought.

The objective of the present paper is to present numerical results obtained via a finite difference numerical technique to solve the problem of fluid flow through a heterogeneous rotating porous channel over a wide range of Ekman number values, leading to distinct flow regimes. This is accomplished by applying a co-ordinate transform that allows mesh refinement to be tailored to the boundary layer position and thickness for each value of Ek under study.

2. PROBLEM FORMULATION

The axial flow through a long rotating square channel filled with fluid-saturated porous material is imposed through an axial pressure gradient. The channel rotates about an axis perpendicular to the horizontal walls (Figure 1(a)). With a homogeneous porous medium, the permeability is constant throughout the flow domain resulting in a uniform distribution of the filtration velocity and rotation does not affect the flow. For heterogeneous porous media (the permeability is spatially dependent) a secondary circulation develops. The particular case where the permeability varies only along the vertical co-ordinate is considered here. This assumption is equivalent with the assumption of developed flow in pure fluids (non-porous domains).

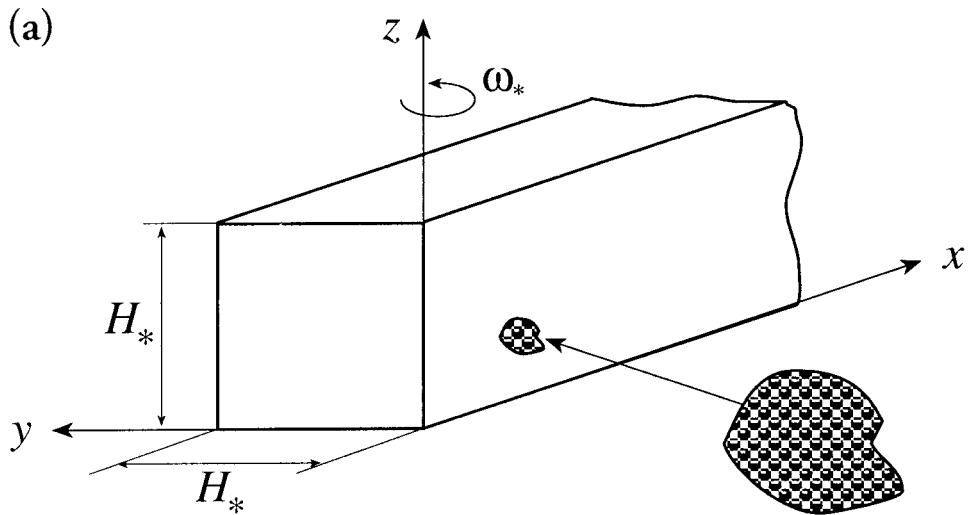
The dimensionless equations governing the flow in a rotating heterogeneous porous media following Darcy's law extended to include the Coriolis and centrifugal terms are presented in the form

(i) Continuity equation

$$\nabla \cdot \mathbf{q} = 0. \tag{1}$$

(ii) Darcy's law (extended to include rotation effects)

$$\mathbf{q} = -k \left[\nabla p_r + \frac{1}{Ek_\Delta} \hat{\mathbf{e}}_\omega \times \mathbf{q} \right]. \tag{2}$$



(b) Permeability Function

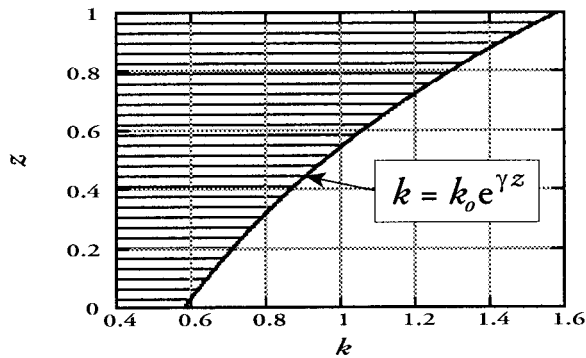


Figure 1. (a) A heterogeneous fluid saturated porous medium in a rotating square channel. (b) Graphical description of the permeability variation within the porous channel.

In Equations (1) and (2), \mathbf{q} is the dimensionless filtration velocity (Darcy's flux), p_r is the dimensionless reduced pressure generalized to include the constant centrifugal as well as the gravity terms, $k(X)$ is the dimensionless permeability function, $\hat{\mathbf{e}}_\omega$ is a unit vector in the direction of the imposed angular velocity and the porous media Ekman number is defined as

$$Ek_\Delta = \frac{\phi v_{c*}}{2\omega_* k_{c*}}, \quad (3)$$

where ϕ is porosity, ω_* is the angular velocity of rotation, k_{c*} is a reference value of permeability and v_{c*} is the kinematic viscosity. The size of the square cross-section of the channel, H_* , is used to transform the independent variables to the following dimensionless form $x = x_*/H_*$, $y = y_*/H_*$, $z = z_*/H_*$. The only dimensionless group that appears in the governing equations is, therefore, the Ekman number (Ek_Δ), which controls the significance of the Coriolis effect. In solving Equations (1) and (2), the following impermeability boundary conditions on the solid walls of the channel apply: $\mathbf{q} \cdot \hat{\mathbf{e}}_n = 0$ on the solid walls, where $\hat{\mathbf{e}}_n$ is a unit vector normal to the channel walls.

It is useful to rescale the variables in Equations (1) and (2) in the form

$$\mathbf{q}^* = \frac{\mathbf{q}}{Ek}, \quad k^* = \frac{k}{Ek}. \quad (4)$$

By applying this scaling, the effect of Ek is absorbed entirely in the definition of k^* , which is then application specific. In doing so, a Cartesian co-ordinate system is used and without loss of generality one can choose $\hat{\mathbf{e}}_\omega = \hat{\mathbf{e}}_z$. Subject to this choice, Equation (2) can be expressed in the following explicit form in terms of its three scalar components (dropping the Δ from Ek_Δ , and the r from p_r for convenience)

$$u^* - k^* v^* = -k^* \frac{\partial p}{\partial x}, \quad (5a)$$

$$v^* - k^* u^* = -k^* \frac{\partial p}{\partial y}, \quad (5b)$$

$$w^* = -k^* \frac{\partial p}{\partial z}. \quad (5c)$$

The only assumption we make is the requirement to have a developed flow along the channel, i.e. $\partial \mathbf{q}^*/\partial x = 0$ everywhere in the channel. This requirement limits the choice of possible permeability variations to variations in the z -direction only. Therefore, $k^* \equiv k^*(z)$, while z is the direction corresponding to the angular velocity of rotation. Although the method described in this paper applies generally to any permeability variation in the z -direction, the computational examples to be presented use an exponential distribution (see Figure 1(b)), of the form

$$k = k_0 e^{\gamma z}. \quad (6)$$

The condition for developed flow in the channel (i.e. $\partial \mathbf{q}^*/\partial x = 0$) implies in particular that $\partial u/\partial x = 0$, thus reducing the continuity equation to the form

$$\frac{\partial v^*}{\partial y} + \frac{\partial w^*}{\partial z} = 0. \quad (7)$$

Equation (7) can be identically satisfied by reformulating the problem via the introduction of a streamfunction, defined in the form $v^* = \partial\psi/\partial z$, $w^* = -\partial\psi/\partial y$. Substituting this definition into Equations (5a)–(5c) yields after some algebraic manipulation

$$\frac{\partial^2\psi}{\partial y^2} + [1 + (k^*)^2] \frac{\partial^2\psi}{\partial z^2} + [(k^*)^2 - 1] \frac{d[\ln(k^*)]}{dz} \frac{\partial\psi}{\partial z} = -k^* \frac{dk^*}{dz} \left(-\frac{\partial p}{\partial x} \right) \quad (8)$$

and

$$u^* = k^* \left[\left(-\frac{\partial p}{\partial x} \right) + \frac{\partial\psi}{\partial z} \right]. \quad (9)$$

As the applied axial pressure gradient is constant, it is convenient to use it as the characteristic pressure gradient and normalize its dimensionless value, i.e. $(-\partial p/\partial x) = 1$. Upon substitution into Equations (8) and (9), this leads to

$$\frac{\partial^2\psi}{\partial y^2} + [1 + (k^*)^2] \frac{\partial^2\psi}{\partial z^2} + [(k^*)^2 - 1] \frac{d[\ln(k^*)]}{dz} \frac{\partial\psi}{\partial z} = -k^* \frac{dk^*}{dz}, \quad (10)$$

$$u^* = k^* \left[1 + \frac{\partial\psi}{\partial z} \right]. \quad (11)$$

Once the function $k(z)$ and the value of Ek are specified ($k^*(z) = k(z)/Ek$), Equation (10) is to be solved subject to the boundary conditions: $\psi = 0$ at $y = 0$, $y = 1$, $z = 0$ and $z = 1$ (impermeable channel walls).

3. NUMERICAL METHOD OF SOLUTION

Early work with a spatially uniform mesh and a simple finite difference scheme indicated that as the Ekman number decreased from 1 to 0.05, the flow in the vertical direction changed from filling the computational domain to confined to a thin region adjacent to the vertical boundaries. The ‘boundary layer flow regime’ at low Ekman numbers suggested a transformation allowing fine and variable discretization near all boundaries and symmetry about both $y = 0.5$ and $z = 0.5$ in the form of

$$y = \frac{r\tilde{y} + (1-r) \left[1 - \frac{\tanh(s(0.5 - \tilde{y}))}{\tanh s} \right] + c_1}{c_2}, \quad (12a)$$

$$z = \frac{r\tilde{z} + (1-r) \left[1 - \frac{\tanh(s(0.5 - \tilde{z}))}{\tanh s} \right] + c_1}{c_2}, \quad (12b)$$

where \tilde{y} and \tilde{z} are the independent variables in the transformed space corresponding to the variables y and z respectively in the true space. In Equations (12a) and (12b), the parameters r and s control the degree and location of mesh refinement, while the scaling constants c_1 and c_2 are chosen to keep the transformed domain boundaries between 0 and 1. Functions similar to those above were used by Eiseman [11,12] to smoothly merge portions of airfoil profiles [11] and then to distribute grid points in attached boundary layers beside the profiles [12]. Eiseman’s second use of the transform was an extension of transforms suggested by Roberts [13] (see also Fletcher [14]). The transform given here is unique in that it allows a finely graded mesh at the two extremes of the computational boundary rather than at a single one. Of the

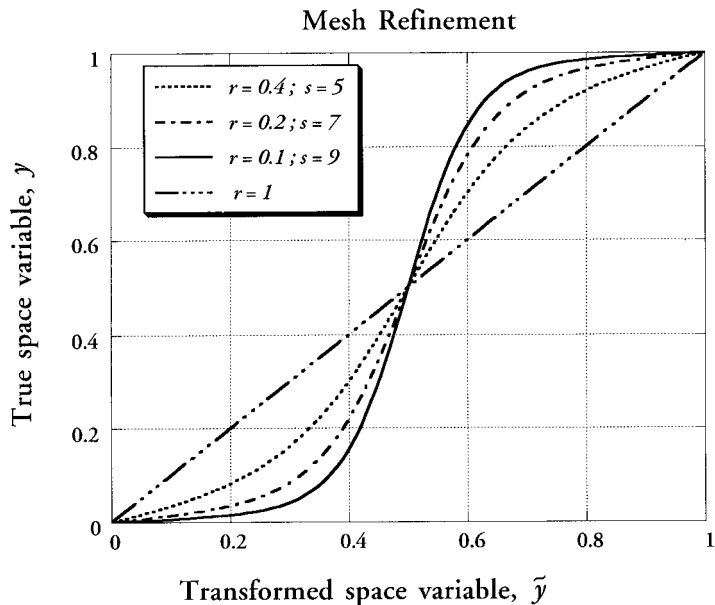


Figure 2. Graphical description of selected transformations of independent variables constituting the mesh refinement technique.

two parameters, r controls the slope of the distribution at the boundary and s (referred to as the damping factor) controls the rate of departure from a linear distribution. The version of the transform cited in Eiseman [11,12] and Fletcher [14] is well-suited to boundary layers in external flows because it allows a finely graded mesh at a wall and a coarse one in the free stream (suited to attached boundary layers). The version given above places a fine mesh at the two extremes of the domain and a coarse mesh in the central region, ideal for the recirculating flow posed here. Note that $r = 1$ leaves the transformed space identical to the true space. The graphical description of selected mesh refinements (i.e. different values of r and s) corresponding to the transformation (12a) and (12b) is presented in Figure 2.

Identical parameters r and s have been used for the two co-ordinate directions in the present work, but the use of two sets should not present significant difficulties. However, as the values for the two sets begin to diverge, one would obtain mesh volumes of increasing aspect ratio. The transform given above has been used with mesh sizes varying from 40×40 to 120×120 . Assuming a 60×60 mesh and $r = 0.4$ and $s = 5$, one obtains eight nodes from the wall to ~ 0.05 , 14 nodes to ~ 0.1 and 22 nodes to ~ 0.25 (a nearly linear distribution that is symmetric about 0.5). This distribution of grid points was typical for the high Ekman number cases ($Ek = 1$) of the present work, where the flow is dispersed throughout the computational domain. For $r = 0.1$ and $s = 9$, one obtains 19 nodes from the wall to ~ 0.05 , 22 nodes to ~ 0.1 and 26 nodes to ~ 0.25 (a strongly non-linear distribution). This distribution of grid points was used for the low Ekman number cases $Ek = 0.05$, where the flow is confined to a very thin layer adjacent to the domain boundaries. For these cases, the entirety of the flow in the vertical direction at the flow boundaries would have been adjacent to the first one or two nodes if a uniformly distributed mesh had been used for the computation.

Application of the transform and the chain rule gives the following governing equation

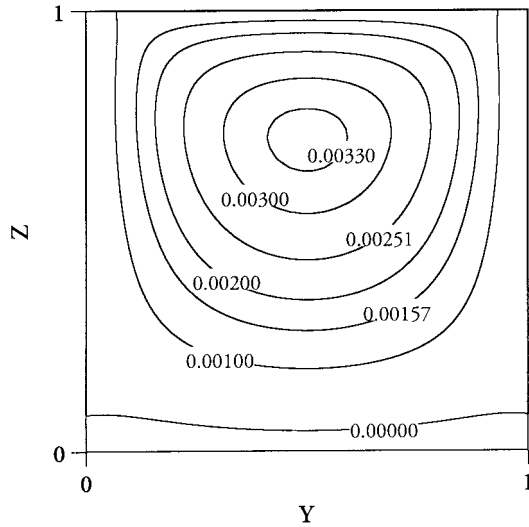


Figure 3. Graphical description of the secondary circulation flow field in terms of streamlines for $Ek = 5$. The domain was divided into 120×120 internal grid points using the mesh refinement transformation parameters $r = 0.2$ and $s = 7$. The maximum value of the streamfunction is $\psi_{\max} = 0.003384$.

$$\begin{aligned} & \frac{\partial^2 \psi}{\partial \tilde{y}^2} \left[\frac{\partial \tilde{y}}{\partial y} \right]^2 + \frac{\partial \psi}{\partial \tilde{y}} \frac{\partial^2 \tilde{y}}{\partial y^2} + [1 + (k^*)^2] \left[\frac{\partial^2 \psi}{\partial z^2} \left[\frac{\partial \tilde{z}}{\partial z} \right]^2 + \frac{\partial \psi}{\partial z} \frac{\partial^2 \tilde{z}}{\partial z^2} \right] + [(k^*)^2 - 1] \frac{1}{k^*} \frac{dk^*}{d\tilde{z}} \frac{\partial \psi}{\partial \tilde{z}} \left[\frac{\partial \tilde{z}}{\partial z} \right]^2 \\ & = -k^* \frac{dk^*}{d\tilde{z}} \frac{\partial \tilde{z}}{\partial z}. \end{aligned} \tag{13}$$

Solutions of this equation are obtained over a uniformly spaced grid in transform space regardless of the choice of r and s parameters (mesh refinement at the boundaries). Evaluation

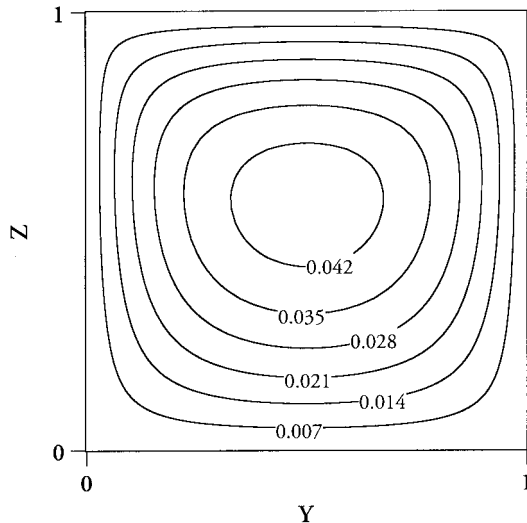


Figure 4. Graphical description of the secondary circulation flow field in terms of streamlines for $Ek = 1$. The domain was divided into 60×60 internal grid points using the mesh refinement transformation parameters $r = 0.4$ and $s = 5$. The maximum value of the streamfunction is $\psi_{\max} = 0.04584$.

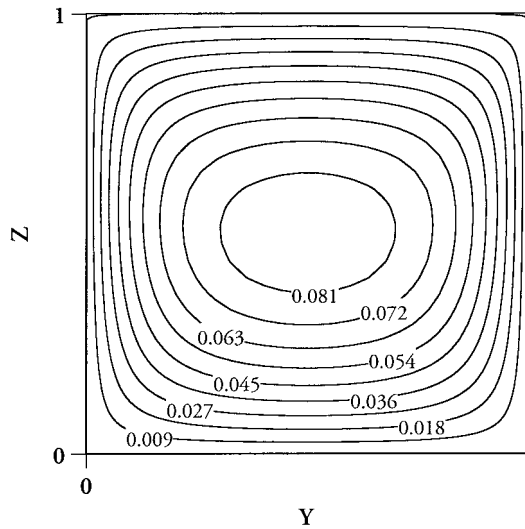


Figure 5. Graphical description of the secondary circulation flow field in terms of streamlines for $Ek = 0.5$. The domain was divided into 60×60 internal grid points using the mesh refinement transformation parameters $r = 0.1$ and $s = 5$. The maximum value of the streamfunction is $\psi_{\max} = 0.08757$.

and substitution of the derivatives of the transforms is straightforward and these are inserted into the numerical scheme in their analytical form. Evaluation and substitution of the derivatives of the spatial dependence of the permeability is easier when done in finite difference form.

The alternating direction implicit (ADI) method (Fletcher [14], Peaceman and Rachford [15]) and second-order-accurate centred finite differences were implemented to solve Equation

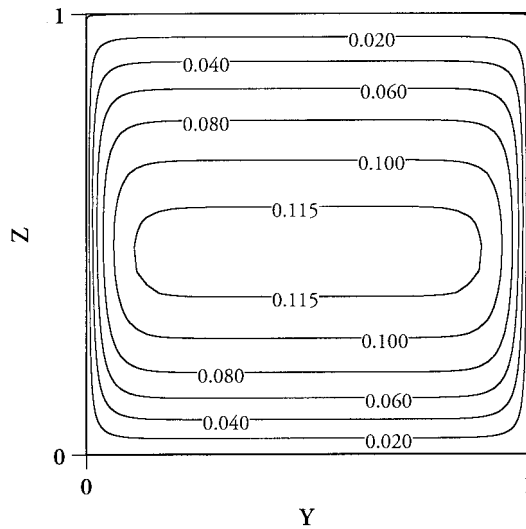


Figure 6. Graphical description of the secondary circulation flow field in terms of streamlines for $Ek = 0.1$. The domain was divided into 60×60 internal grid points using the mesh refinement transformation parameters $r = 0.1$ and $s = 7$. The maximum value of the streamfunction is $\psi_{\max} = 0.1204$.

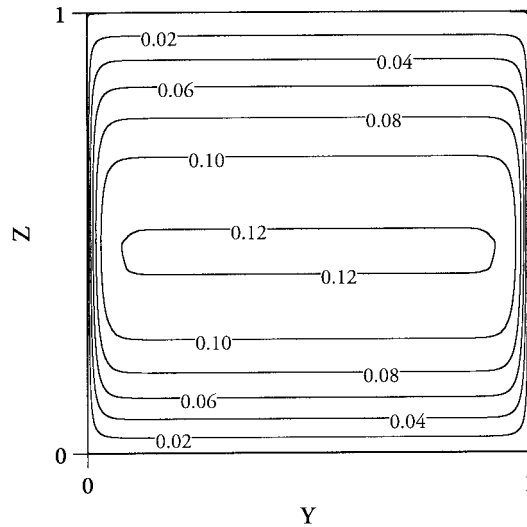


Figure 7. Graphical description of the secondary circulation flow field in terms of streamlines for $Ek = 0.05$. The domain was divided into 60×60 internal grid points using the mesh refinement transformation parameters $r = 0.1$ and $s = 7$. The maximum value of the streamfunction is $\psi_{\max} = 0.1215$.

(13). A single relaxation parameter was used with the Thomas algorithm solution of each tridiagonal stage. Cyclical usage of a set of relaxation parameters was tried but was slower than using a single relaxation parameter with repeated reuse of the LU decomposition. Iteration was terminated when the fractional change in the streamfunction was less than 1.0×10^{-7} at all grid points. As a consistency check, the error in the governing equation as a fraction of the sum of the absolute value of the six terms in Equation (13) was computed for each grid point and the maximum value reported with the results for each Ekman number

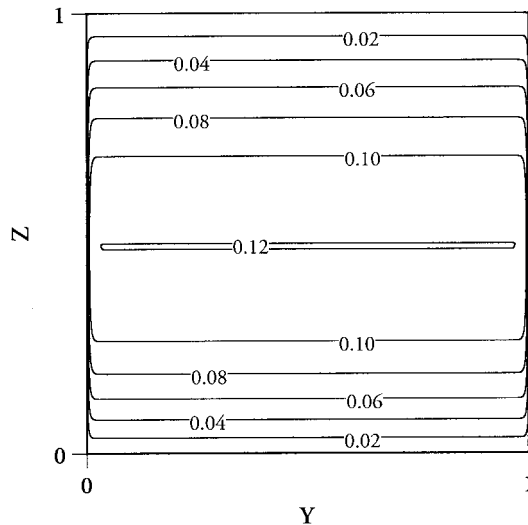


Figure 8. Graphical description of the secondary circulation flow field in terms of streamlines for $Ek = 0.01$. The domain was divided into 60×60 internal grid points using the mesh refinement transformation parameters $r = 0.08$ and $s = 6.5$. The maximum value of the streamfunction is $\psi_{\max} = 0.1221$.

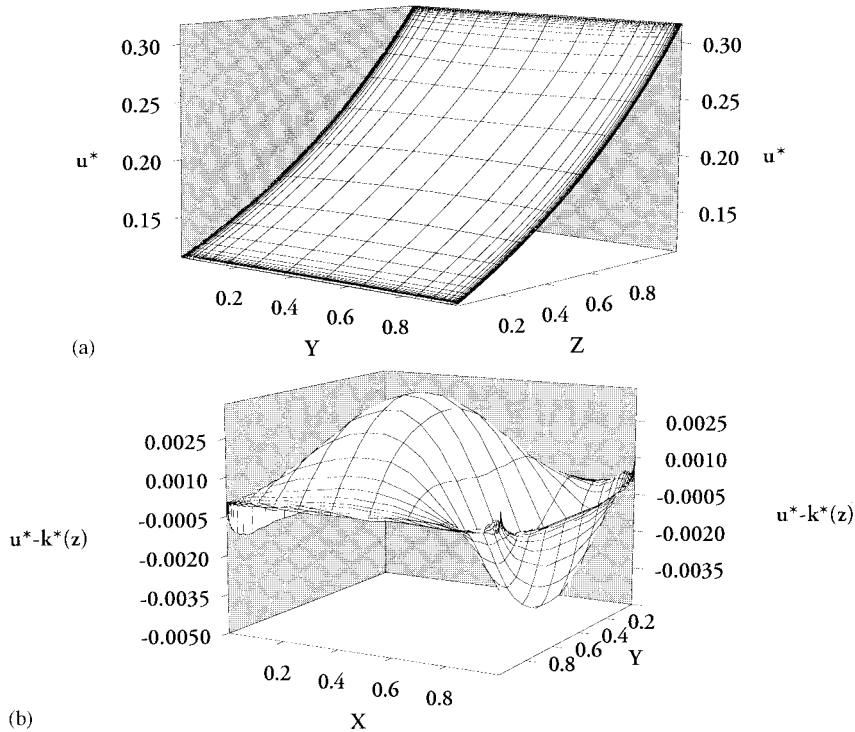


Figure 9. (a) Graphical description of the axial flow field $u^*(y, z)$ for $Ek = 5$. The results correspond to a division of the channel cross-section into 60×60 internal grid points using the mesh refinement transformation parameters $r = 0.1$ and $s = 9$. (b) Graphical description of the impact of rotation on the axial flow expressed by the deviation of the axial flow field from the corresponding flow in the absence of rotation, i.e. $u^* - u_0^* \equiv u^* - k^*(z)$.

investigated. Further tests performed to establish the effectiveness of the mesh refinement used, and the grid independence of the results are presented at the end of the next section.

4. RESULTS AND DISCUSSION

The exponential permeability function presented in Equation (6) and used throughout causes the coefficient $d[\ln(k^*)]/dz$, of $\partial\psi/\partial z$ in Equation (10) to be a constant. For high values of Ek an expansion in terms of Ek^{-1} produces a linear equation with constant coefficients, which has analytical solutions of the form presented by Vadasz [10]. Using the same exponential permeability function as in Vadasz [10] permits a comparison, at least qualitatively, between the numerical solution and the approximate analytical results (which apply when $Ek \gg 1$). In order to facilitate comparisons between results for a variety of permeability functions, k_0 and γ in Equation (6) are selected to produce a unit value of flow rate for the no-rotation condition. When rotation is absent, $Ek \rightarrow \infty$, $u = u_0(z) = k(z)$, so that

$$Q = \int_0^1 \int_0^1 u(z) \, dy \, dz = \int_0^1 dy \int_0^1 k(z) \, dz = \int_0^1 k(z) \, dz. \tag{14}$$

For a homogeneous channel $k = 1$ and the flow rate is $Q = 1$. To get the same flow rate with the exponential permeability function, we require $k_0(e^\gamma - 1) = \gamma$. Since there are infinitely many

pairs of (γ, k_0) that fulfil this condition, we chose $\gamma = 1$, which uniquely determines the permeability function: $k(z) = 0.582 e^z$. It is important to notice that the choice of a monotonic-type of permeability function indicates that the secondary flow in the y - z plane is expected to be consistent with a positive permeability gradient, i.e. the direction of the vortex flow is anticipated to be anticlockwise for all cases corresponding to this permeability function. This expectation is based on the analytical results presented by Vadasz [10]. From eight to 12 computer runs were performed for each value of Ekman number and the best numerical mesh refinement parameters and number of internal grid points were identified. We present here only a selected number of results to highlight the wide applicability of the method over Ekman number values ranging from $Ek = 5$, corresponding to slow rotation rates, and down to $Ek = 0.01$ corresponding to high rotation rates.

The streamlines for the secondary circulation in the y - z plane for $Ek = 5$ are presented in Figure 3. The unicellular flow is counterclockwise as expected, with some boundary layer identified with sharper gradients and consequently higher filtration velocity, v^* , developing along the upper wall. The flow field is substantially asymmetric with respect to $z = 0.5$ but perfectly symmetric in the y -direction, i.e. with respect to $y = 0.5$. As the rotation rate becomes moderate, corresponding to $Ek = 1$, which is presented in Figure 4, the gradients become moderate as well and less asymmetric in the z -direction. Graphical description of the results associated with a further reduction in the value of Ekman number, i.e. $Ek = 0.5$, is presented

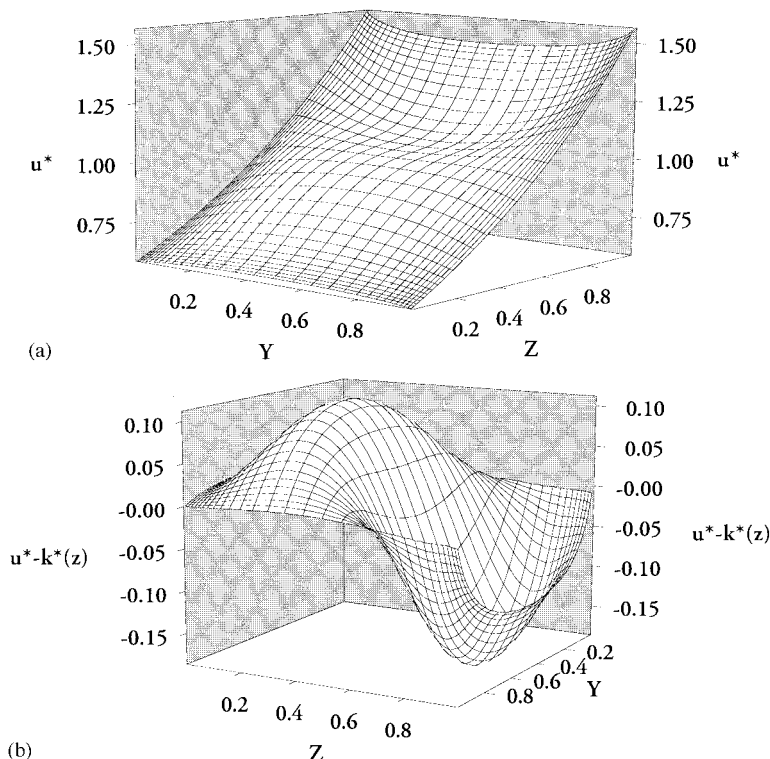


Figure 10. (a) Graphical description of the axial flow field $u^*(y, z)$ for $Ek = 1$. The results correspond to a division of the channel cross-section into 60×60 internal grid points using the mesh refinement transformation parameters $r = 0.4$ and $s = 5$. (b) Graphical description of the impact of rotation on the axial flow expressed by the deviation of the axial flow field from the corresponding flow in the absence of rotation, i.e. $u^* - u_0^* \equiv u^* - k^*(z)$.

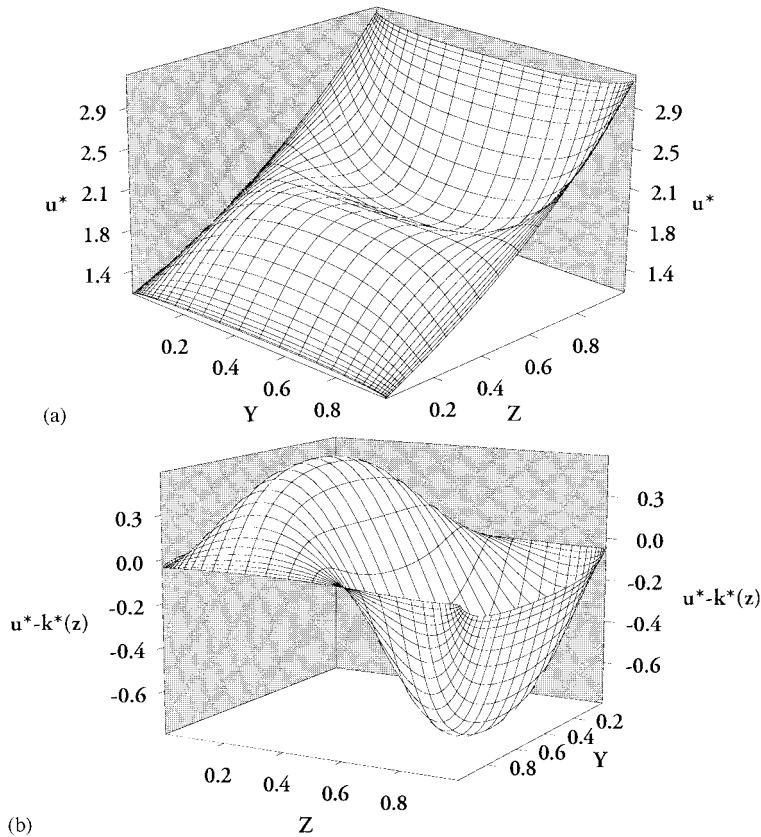


Figure 11. (a) Graphical description of the axial flow field $u^*(y, z)$ for $Ek = 0.5$. The results correspond to a division of the channel cross-section into 60×60 internal grid points using the mesh refinement transformation parameters $r = 0.1$ and $s = 5$. (b) Graphical description of the impact of rotation on the axial flow expressed by the deviation of the axial flow field from the corresponding flow in the absence of rotation, i.e. $u^* - u_0^* \equiv u^* - k^*(z)$.

in Figure 5, where an almost perfect symmetry in the z - as well as in y -directions can be observed. Figure 6 presents the streamline results for $Ek = 0.1$, which show that the streamlines become almost horizontal in the core of the cross-section and development of boundary layers is identified along the vertical walls at $y = 0$ and $y = 1$. A break of vertical symmetry can also be identified as well. As the Ekman number becomes small, the graphical results presented in Figure 7 for $Ek = 0.05$ show that the vertical boundary layers are well-developed and the core region where the streamlines are horizontal occupies most of the flow domain. A further reduction of the Ekman number to $Ek = 0.01$ yields very narrow vertical boundary layers next to the vertical walls, while most of the domain has horizontal streamlines (Figure 8). The appearance of horizontal streamlines in the interior is associated with a zero value of the vertical component of the filtration velocity, i.e. $w^* = 0$ in the interior. This result is a consequence (and reconfirmation) of the Taylor–Proudman theorem in porous media, which was demonstrated theoretically and confirmed experimentally by Vadasz [1], and reaffirms the anticipation of a geostrophic-type of flow at small values of Ekman number.

Since the objective of the paper is to investigate the Coriolis effect on the axial flow in the channel, which is expressed by the term $(-\boldsymbol{\omega} \times \mathbf{q})$ in the extended Darcy’s equation, it is evident that the secondary circulation in the y - z plane is the result of the cross product

($-\hat{e}_z \times u\hat{e}_x$). However, as soon as this secondary flow in the y - z plane is established it influences the original axial flow in the channel through the Coriolis components ($-\hat{e}_z \times v\hat{e}_y$) and ($-\hat{e}_z \times w\hat{e}_z$). Therefore, in order to observe this effect, three-dimensional surface plots of the resulting axial flow field $u^*(y, z)$ are presented in Figures 9(a)–14(a). To observe the isolated effect of the rotation on the axial flow we present the results of the deviation of $u^*(y, z)$ from its corresponding value associated with the case without rotation, i.e. $u_0^*(z) \equiv k^*(z)$, in Figures 9(b)–14(b). The surface plot of $u^*(y, z)$ for $Ek = 5$ (i.e. corresponding to the streamlines presented in Figure 3) is presented in Figure 9(a), where it appears that the axial filtration velocity follows the shape of the permeability function. However, the impact of rotation is detected in Figure 9(b), where the deviation of $u^*(y, z)$ from $k^*(z)$ shows a distinct effect that accounts for about 20% of the value of $u^*(y, z)$. Stronger rotational effects are presented in Figure 10(a), corresponding to $Ek = 1$, where an axial flow deficiency is observed on the top half of the channel and an axial flow enhancement appears in the bottom half. The deviation of $u^*(y, z)$ from its irrotational value clearly identifies this effect as presented in Figure 10(b). The same effect becomes stronger as the Ekman number decreases to $Ek = 0.5$ as presented in Figure 11(a) and (b), where it can be observed that in the vicinity of the vertical walls (i.e. at $y = 0$ and $y = 1$), the effect of rotation is neutralized. At $Ek = 0.1$ (Figure 12(a) and (b)) this effect is so strong that the vertical boundary layers are clearly identified in the

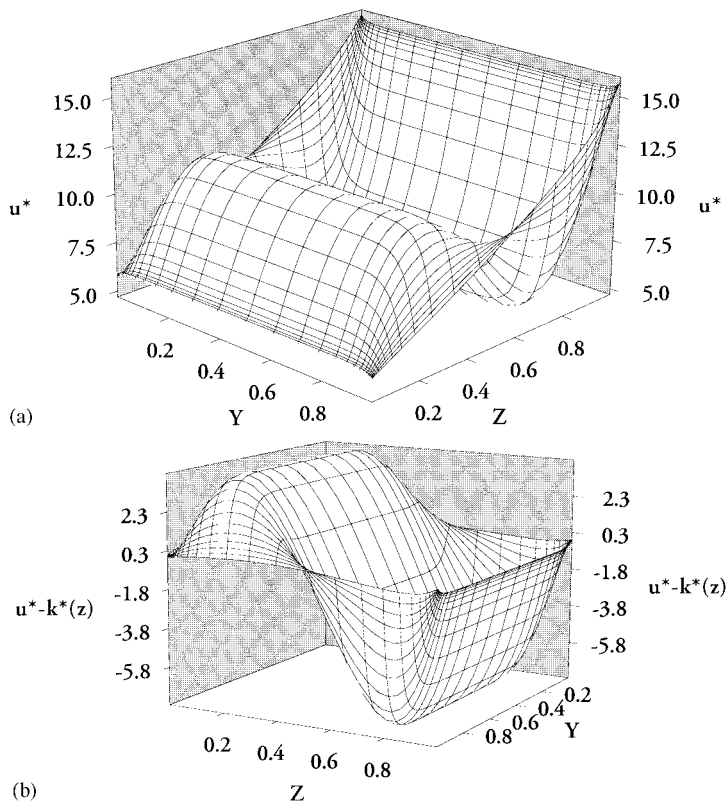


Figure 12. (a) Graphical description of the axial flow field $u^*(y, z)$ for $Ek = 0.1$. The results correspond to a division of the channel cross-section into 60×60 internal grid points using the mesh refinement transformation parameters $r = 0.1$ and $s = 7$. (b) Graphical description of the impact of rotation on the axial flow expressed by the deviation of the axial flow field from the corresponding flow in the absence of rotation, i.e. $u^* - u_0^* \equiv u^* - k^*(z)$.

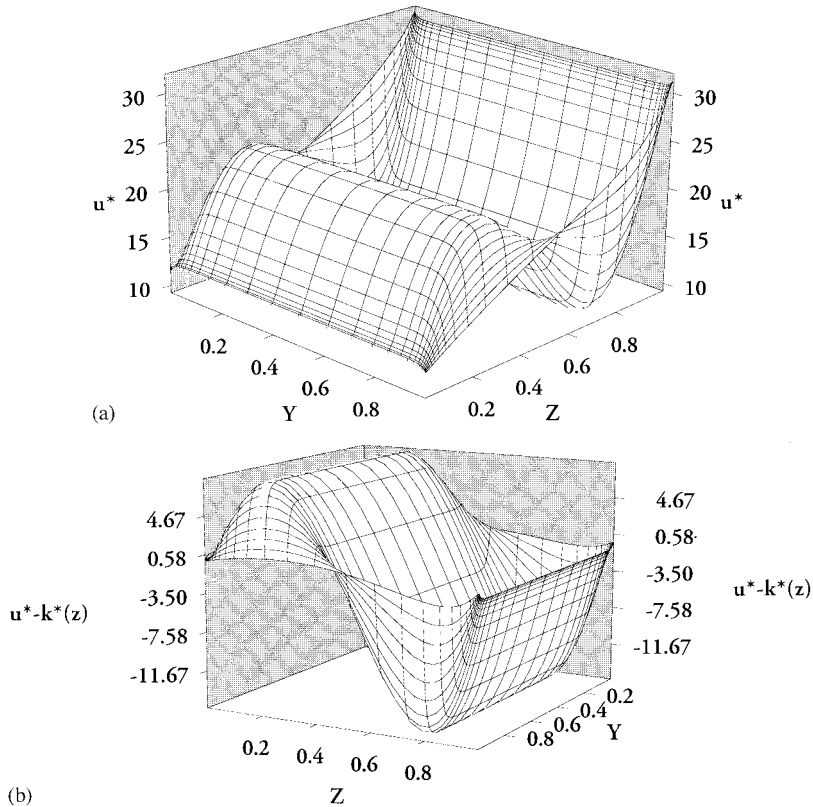


Figure 13. (a) Graphical description of the axial flow field $u^*(y, z)$ for $Ek = 0.05$. The results correspond to a division of the channel cross-section into 60×60 internal grid points using the mesh refinement transformation parameters $r = 0.1$ and $s = 7$. (b) Graphical description of the impact of rotation on the axial flow expressed by the deviation of the axial flow field from the corresponding flow in the absence of rotation, i.e. $u^* - u_0^* \equiv u^* - k^*(z)$.

axial filtration velocity surface plot and the velocity field shape resembles a bucket. This shape and the corresponding vertical boundary layers become more pronounced in Figure 13(a) and (b), corresponding to $Ek = 0.05$, and again in Figure 14(a) and (b), corresponding to $Ek = 0.01$.

The thin boundary layers obtained in small Ekman number cases suggest the evaluation of a boundary layer thickness. For flow in pure fluids (non-porous domains) the concept of boundary layer thickness is obvious and its definitions are well-established but there is no analogous formulation for flow in porous media where the tangent filtration velocity component at the solid walls does not vanish, i.e. there is slip on the solid walls (actually, the results here show that the vertical filtration velocity component is maximum at the vertical walls). In this work we define a boundary layer thickness that is to some degree similar to the boundary layer displacement thickness in pure fluids (non-porous domains). The boundary layer thickness δ , is the distance in the y -direction that is required at the maximum velocity of the vertical flow to get the same flow rate as actually computed for the vertical flow:

$$\delta w^*|_{y=0} = \int_0^{0.5} w^* dy. \tag{15}$$

The value of z where w^* is evaluated is the location where the streamfunction is maximum, i.e. the value of z where ψ_{\max} occurs. As with the conventional boundary layer thickness, δ represents a thickness into which the flow velocity gradients near a wall are integrated. Substituting for $w^* = -\partial\psi/\partial y$ in Equation (15) gives δ in terms of the streamfunction in the form

$$\delta = \frac{\int_0^{0.5} w^*(y) dy}{w^*|_{y=0}} = \frac{-1}{w^*|_{y=0}} \int_0^{0.5} \frac{\partial\psi}{\partial y} dy = \frac{[\psi|_{y=0} - \psi|_{y=0.5}]}{w^*|_{y=0}}. \quad (16)$$

The computational results for boundary layer thickness evaluated using Equation (16) are presented by the discrete points in Figure 15. A power law fit of the thickness as a function of Ekman number in the form $\delta = aEk^b$ gives $a = 0.22$ and $b = 0.72$. Clearly the fit is better for small Ekman numbers and deviates quite significantly from the computed boundary layer thickness results as Ekman number increases but it is for small values of Ekman number that a boundary layer flow regime is observed and the concept has utility.

Further tests for establishing grid independence of the numerical results were undertaken and are presented in Figure 16, in terms of the boundary layer thickness, δ , as a function of

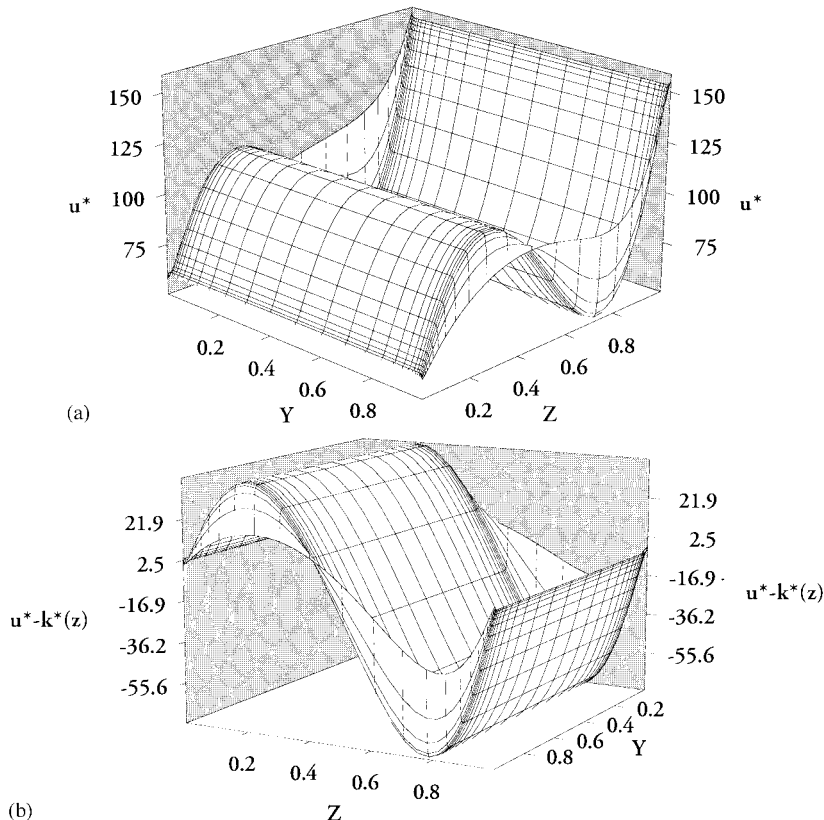


Figure 14. (a) Graphical description of the axial flow field $u^*(y, z)$ for $Ek = 0.01$. The results correspond to a division of the channel cross-section into 60×60 internal grid points using the mesh refinement transformation parameters $r = 0.08$ and $s = 6.5$. (b) Graphical description of the impact of rotation on the axial flow expressed by the deviation of the axial flow field from the corresponding flow in the absence of rotation, net $u^* - u_0^* \equiv u^* - k^*(z)$.

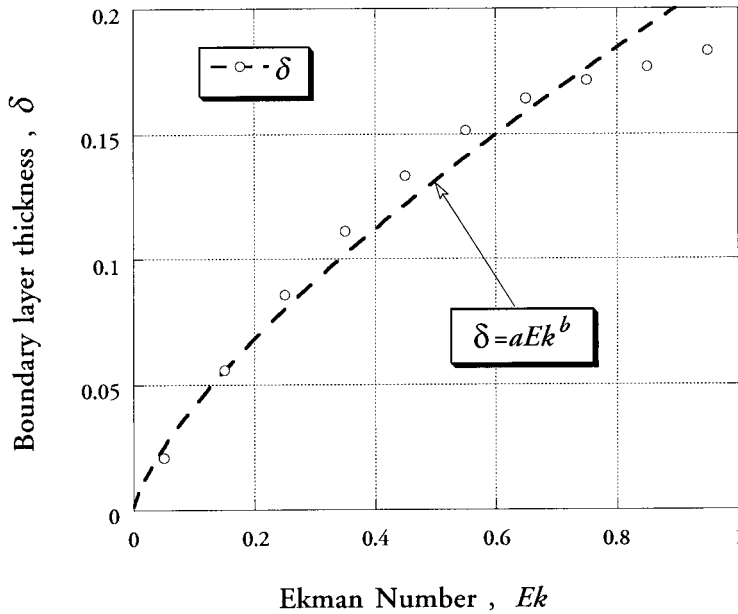


Figure 15. The computed results of the boundary layer thickness vs. Ekman number and the closest power-law correlation with the computed results.

the grid size for different combinations of the parameters controlling the degree and location of the mesh refinement, r and s . All these tests apply to a value of $Ek = 0.05$, while the choice of the values of r and s for the presentation in Figure 16 was guided by the desire to have a

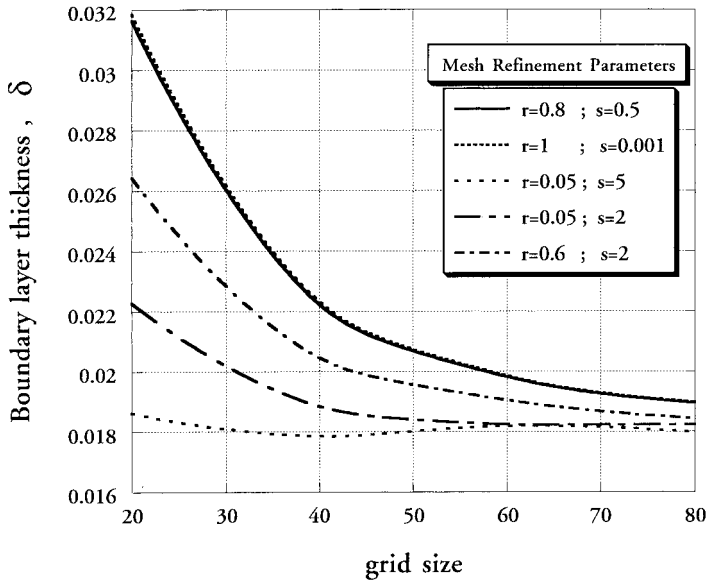


Figure 16. Mesh refinement and grid independence tests results for $Ek = 0.05$. The boundary layer thickness, δ , as a function of the grid size for different combinations of the parameters controlling the degree and location of the mesh refinement, r and s .

few well-spaced curves on the plot. The curves corresponding to other intermediate values of r and s are located just in-between the curves presented. These curves in Figure 16 indicate clearly that the calculated boundary layer thickness converges well already at a mesh size of 80×80 , while a careful choice of the mesh refinement parameters can reduce significantly the mesh size without affecting the accuracy of the results. The numerical results previously presented followed this procedure regarding the best choice of mesh refinement parameters to minimize the mesh size while maintaining numerical accuracy.

5. CONCLUSIONS

The numerical solution to the problem of the three-dimensional fluid flow in a long rotating porous channel show distinct flow regimes as the porous media Ekman number varies over a wide range of values. At high values of Ekman numbers horizontal boundary layers in the vicinity of the horizontal walls appear while as the value of Ekman number decreases vertical boundary layers appear next to the vertical walls and they become more pronounced as Ekman number becomes very small. The results confirm that the secondary flow in a plane perpendicular to the imposed axial flow (resulting from rotation) depends strongly on the variation of the permeability. Geostrophic flow in the core region of the channel is also reaffirmed for small values of Ekman number. The numerical results permitted the evaluation of a power-law correlation of the boundary layer thickness to Ekman number for small values of the latter, which is shown to be a simple and practical way to estimate the boundary layer thickness.

ACKNOWLEDGMENTS

The authors wish to thank the Foundation for Research Development (South Africa) for partially supporting this study through the Competitive Industry Research Grant (CIPM-GUN2034039).

APPENDIX A. NOMENCLATURE

- Ek Ekman number, defined by Equation (3)
- \hat{e}_x unit vector in the x -direction
- \hat{e}_y unit vector in the y -direction
- \hat{e}_z unit vector in the z -direction
- \hat{e}_n unit vector normal to the solid boundary, positive outwards
- \hat{e}_ω unit vector in the direction of the angular velocity of rotation
- H^* the size of the square cross-section of the channel
- k dimensionless permeability function
- k_c^* a reference value of permeability, dimensional
- p pressure, dimensionless
- \mathbf{q} filtration velocity, dimensionless
- Q volumetric flow rate, dimensionless
- r a parameter controlling the mesh refinement
- s a parameter controlling the mesh refinement
- u horizontal x component of the filtration velocity
- u_0 horizontal x component of the filtration velocity in the absence of rotation.

- v horizontal y component of the filtration velocity
 w vertical component of the filtration velocity
 \mathbf{X} position vector, equals $x\hat{e}_x + y\hat{e}_y + z\hat{e}_z$
 x horizontal length co-ordinate
 y horizontal width co-ordinate
 \tilde{y} horizontal width co-ordinate in the transformed space
 z vertical co-ordinate
 \tilde{z} vertical co-ordinate in the transformed space

Greek letters

- δ boundary layer thickness
 ϕ porosity
 ω_* angular velocity of the rotating porous domain
 ν_{c*} fluid's kinematic viscosity, dimensional
 ψ streamfunction

Subscripts

- $*$ dimensional values
 c characteristic values

Superscripts

- $*$ rescaled dimensionless variables, applies to filtration velocity and permeability

REFERENCES

1. P. Vadasz, 'Flow in rotating porous media', in J.P. du Plessis (ed.), *Advances in Fluid Mechanics: Fluid Transport in Porous Media*, Computational Mechanics Publications, Southampton, 1997, Chapter 4, pp. 161–214.
2. A.B. Whitehead, 'Distributor characteristics and bed properties', in J.F. Davidson, R. Clift and D. Harrison (eds.), *Fluidization*, 2nd edn., Academic Press, London, 1985, pp. 173–199.
3. J.F. Davidson and D. Harrison, *Fluidised Particles*, Cambridge University Press, Cambridge, 1963, p. 7.
4. V.B. Kvasha, 'Multiple-spouted gas-fluidized beds and cyclic fluidization: operation and stability', in J.F. Davidson, R. Clift and D. Harrison (eds.), *Fluidization*, 2nd edn., Academic Press, London, 1985, pp. 675–701.
5. L. Katgerman, 'Heat transfer phenomena during continuous casting of aluminium alloys', *Proc. 10th Int. Heat Transfer Conference*, SK-12, Brighton, UK, 1994, pp. 179–187.
6. S.I. Güçeri, 'Fluid flow problems in processing composites materials', *Proc. 10th Int. Heat Transfer Conference*, vol. 1, Brighton, UK, 1994, pp. 419–432.
7. D.A. Nield and A. Bejan, *Convection in Porous Media*, 2nd edn., Springer, New York, 1999.
8. A. Bejan, *Convection Heat Transfer*, 2nd edn., Wiley, New York, 1995.
9. J. Bear, *Dynamics of Fluids in Porous Media*, Elsevier, New York, 1972, pp. 131–132.
10. P. Vadasz, 'Fluid flow through heterogeneous porous media in a rotating square channel', *Transp. Porous Media*, **12**, 43–54 (1993).
11. P. Eiseman, 'A co-ordinate system for a viscous transonic cascade analysis', *J. Comput. Phys.*, **26**, 307–338 (1978).
12. P. Eiseman, 'A multi-surface method of co-ordinate generation', *J. Comput. Phys.*, **33**, 118–150 (1979).
13. G. Roberts, 'Computational meshes for boundary layer problems', in *Proc. 2nd Int. Conf. on Numerical Methods in Fluid Dynamics*, Springer, New York, 1971, pp. 171–177.
14. C.A.J. Fletcher, *Computational Techniques for Fluid Dynamics*, Springer, Berlin, 1991, 104–106.
15. D. Peaceman and H. Rachford, 'The numerical solution of parabolic and elliptic differential equations', *SIAM J.*, **3**, 28–41 (1955).